Continental Shelf Research 60S (2013) S125–S135

Contents lists available at SciVerse ScienceDirect

Continental Shelf Research

journal homepage: www.elsevier.com/locate/csr

Research papers

Thermal observations of drainage from a mud flat

J. Paul Rinehimer [a,b,*], Jim Thomson [a,b], C. Chris Chickadel [a]

[a] Applied Physics Lab, University of Washington, United States
[b] Civil and Environmental Engineering, University of Washington, United States

ARTICLE INFO

Article history:
Received 25 February 2012
Received in revised form
15 October 2012
Accepted 1 November 2012
Available online 9 November 2012

Keywords:
Tidal flats
Remote sensing
Infrared

ABSTRACT

Incised channels on tidal flats create a complex flow network conveying water on and off the flat during the tidal cycle. In situ and remotely sensed field observations of water drainage and temperature in a secondary channel on a muddy tidal flat in Willapa Bay, Washington (USA) are presented and a novel technique, employing infrared imagery, is used to estimate surface velocities when the water depth in the channel becomes too shallow for ADCP measurements, i.e., less than 10 cm. Two distinct dynamic regimes are apparent in the resulting observations: ebb-tidal flow and the post-ebb discharge period. Ebb tide velocities result from the surface slope associated with the receding tidal elevation whereas the post-ebb discharge continues throughout the low tide period and obeys uniform open-channel flow dynamics. Volume transport calculations and a model of post-ebb runoff temperatures support the hypothesis that remnant water on the flats is the source of the post-ebb discharge.

1. Introduction

Fine-grained intertidal flats provide habitat for many aquatic species and economic value for fisheries, but their complex environment makes field observations of water and sediment dynamics difficult. Variations in water depth during the tide transform the hydrodynamic environment between a shallow embayment at high tide and a drainage basin at low tide (Le Hir et al., 2000). Within this complex spatial arrangement and varying scales of motion, incised channels convey water and sediment throughout the system (Ralston and Stacey, 2007). It is well known that channels play an important role in the later stages of receding ebb tidal flow (Wood et al., 1998; Nowacki and Ogston, 2013) conveying water on the flats downstream. Water continues to flow out through these channels long after the ebb tide has passed (i.e., after the tide water is below a given location on the flats) (Whitehouse et al., 2000). Although this 'post-ebb discharge' is common, there has been limited quantitative description or dynamic understanding of these flows.

Recent work suggests that post-ebb discharge in channels results from the runoff of remnant water on the surface of the tidal flat (Mariotti and Fagherazzi, 2011; Whitehouse et al., 2000; Allen, 1985) and that runoff patterns control the distribution of many aquatic species (Gutiérrez and Iribarne, 2004). Other studies suggest the post-ebb drainage results from porewater discharge from with the flats, although it is a much slower process (Anderson and Howell, 1984). From either source, these studies agree that post-ebb drainage can be an important mechanism for the transport of water, sediment, and heat.

The drainage of remnant surface water via nearly parallel, ridge-separated channels located on the flat surface called runnels may be particularly important for off-flat transport (Fagherazzi and Mariotti, 2012; Gouleau et al., 2000). Thus, a mass budget for a tidal flat system is incomplete without quantification of post-ebb drainage. For example, in a study of a nearby channel in Willapa Bay, Nowacki and Ogston (2013) find that an equilibrium sediment budget requires additional export that is missing from their analysis of purely tidal flows. Although post-ebb channel discharge appears small by qualitative (visual) observation, recent work by Fagherazzi and Mariotti (2012) has shown that shear stresses due to this process are higher than the critical stress for erosion and that suspended sediment concentrations are greater than during tidal flows. Kleinhans et al. (2009) found post-ebb surface velocities of 0.1–0.2 ms^{-1} and showed that the post-ebb flow controlled channel meandering, as well as bank and backward step erosion in the incised channels.

Estimation of channel discharge requires knowledge of depth and cross-sectionally averaged velocities at all stages of the drainage. One reason that post-ebb drainage has not been well described is the difficulty in measuring very shallow (depth less than 10 cm) flows. Here, we utilize a novel technique to measure shallow flows remotely with infrared (IR) images. The IR method is combined with conventional acoustic Doppler measurements during periods of greater depth, and there is good agreement between the two approaches during these periods. The integration of these data sets provides a continuous time series of the channel discharge velocities.

* Corresponding author at: Applied Physics Lab, University of Washington, United States. Tel.: +1 206 616 5736.
E-mail address: jprine@apl.washington.edu (J. Paul Rinehimer).

0278-4343/$ - see front matter © 2012 Elsevier Ltd. All rights reserved.
http://dx.doi.org/10.1016/j.csr.2012.11.001

Furthermore, the IR imagery measures the horizontal (cross-channel) variations in surface velocity allowing greater detail in the flow structure to be observed in addition to the vertical velocity profiles from the in situ measurements. Parametric fits for these profiles are then used to make continuous estimates of the volume flux discharged from the channel.

In addition to describing the structure and magnitude of the channel drainage, we compare the temperature of the drainage water to a model prediction for the temperature of remnant surface water (i.e., the hypothetical source of the post-ebb drainage). The model formulation follows Kim et al. (2010), in which the terms of surface heat fluxes are prescribed and the heat exchange between water and sediment is modeled explicitly. The model predicts remnant surface water temperatures that match the observed drainage temperatures and thus support the hypothesis of surface runoff. The corresponding total transport of heat is placed in context with previous observations of low tide heat budgets in muddy tidal flats.

2. Methods

2.1. Site description

Willapa Bay, Washington (Fig. 1) is located on the Pacific coast of the United States, north of the Columbia River mouth. The Long Beach peninsula separates the estuary from the ocean with an 8-km-wide inlet at the northern end of the bay. The tide is mixed semidiurnal with a mean daily range of 2.7 m, varying between 1.8 m (neap) and 3.7 m (spring). The intertidal zone occupies nearly half of the bay's surface area (Andrews, 1965) and almost half of the bay's volume is flushed out of the bay each tide (Banas et al., 2004). Extensive tidal flats occupy much of the bay's intertidal region. Silt and clay sediment predominates in the southern bay and lower energy environments, while fine sand flats are found in higher energy areas, such as along the major channels and locations exposed to waves (Peterson et al., 1984).

The study site is located at the mouth of "D channel" (46° 23′ 26.12″ N, 123° 57′ 43.26″ W) in the southern portion of the bay near the Bear River Channel. The Bear River Channel is the tidal extension of the Bear River which drains into the bay approximately 2 km south of D channel. D channel is a branching, dead end channel (Ashley and Zeff, 1988) that drains 0.3 km^2 of tidal flats into the Bear River channel. At our study site, the channel is incised into the flat about 0.7–1 m deep and 1–2 m wide.

The focus of study is a single spring tide on 31 March 2010. Lower-low water occurred at 10:00 (all times referenced in this paper are local, Pacific Daylight Time) while the period where the regional water level was below the mouth of D channel and all the surrounding flats exposed, (see Fig. 1), lasted approximately 1.5 h, from 09:15 to 10:45. During this period water was observed to continually drain out from D channel. We define this as the 'post-ebb discharge', because the ebb tide effectively finished (i.e., passed the site) at 09:15

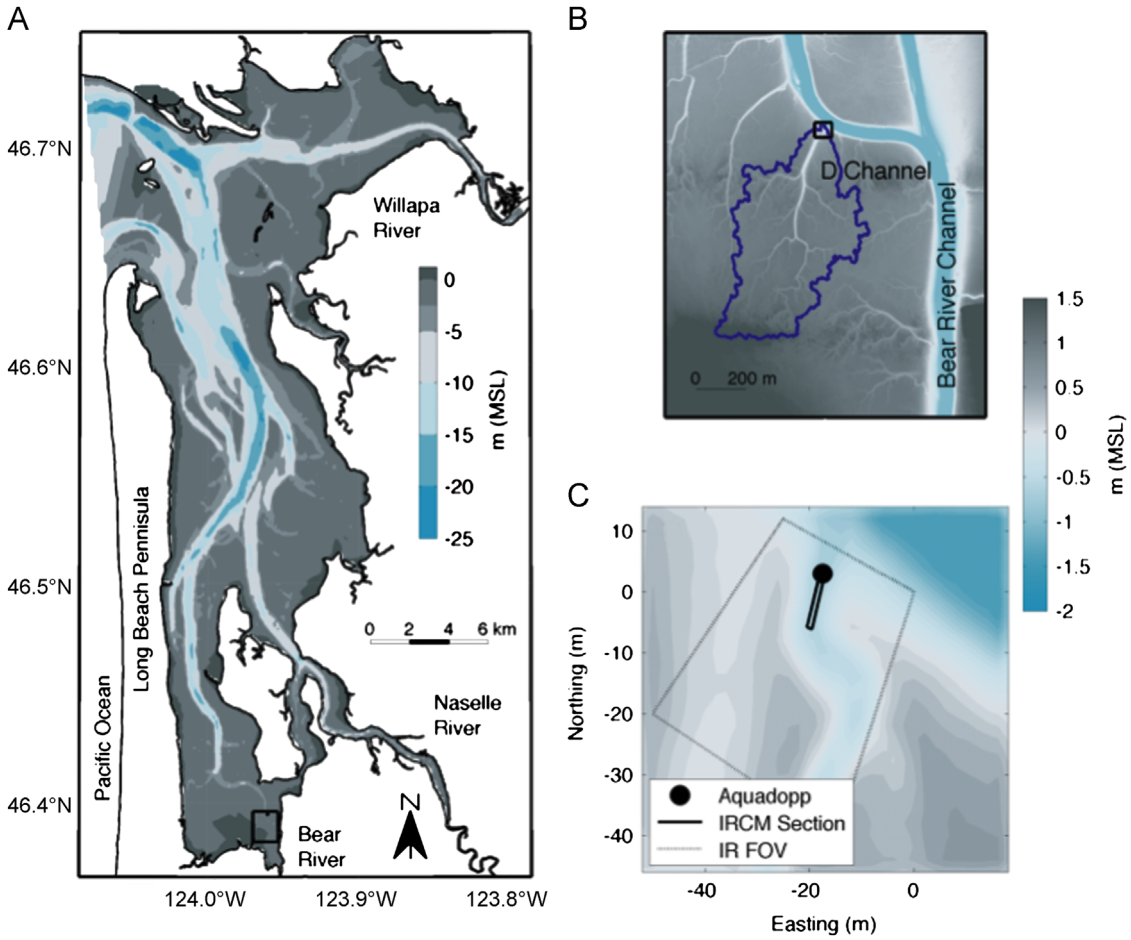

Fig. 1. (a) Willapa Bay bathymetry. The black box indicates the region of sub panel (b) bathymetry of D channel from LiDAR survey and the calculated drainage area. The black box indicates the D channel mouth shown in (c) Close-up of D channel mouth with locations of field instruments. The circle indicates the location of the Aquadopp ADCP, the line is where the IRCM timeslices were taken (see Section 2), and the trapezoid is the infrared camera field of view from the imaging tower at the local origin [0,0]. Bathymetry for (a) is indicated by the inset color bar whereas the right color bar shows the scale for (b) and (c).

and the flood tide did not inundate D channel until 10:45. This period is distinct from the ebb-tide pulse which occurred earlier (approximately 08:00) when the tidal elevation was near the flat elevation.

2.2. In situ measurements: velocity, temperature, and meteorology

A bed-mounted uplooking 2 MHz Nortek Aquadopp Acoustic Doppler Current Profiler (ADCP) located at the mouth of D-Channel recorded velocity profiles at 1 Hz with a vertical resolution of 3 cm and a 10 cm blanking distance. The Aquadopp was used in HR (high resolution) pulse coherent mode to obtain fine-scale vertical resolution, with a vertical profiling distance of 1 m. Aquadopp measurements with a pulse correlation below 40 (out of 100) are excluded from analysis, as are the two bins nearest the surface water level (as determined from the Aquadopp pressure gauge). The Aquadopp also measured water temperature in the channel.

Meteorological data were collected from an Onset HOBO meteorological station mounted to a piling at the mouth of D channel, as well as from a Washington State University AgWeatherNet station approximately 5.5 km southwest of D channel (on land). Meteorological data include rainfall, which is known to enhance runoff from tidal flats (Uncles and Stephens, 2011). For the period surrounding the low tide of 31 March 2010, there was trace rainfall (less than 0.25 mm) during two 15 min periods for a maximum possible rainfall of 0.5 mm.

Time series of sediment temperature profiles were collected with ONSET HOBO Temp Pro v2 temperature data loggers mounted on sand anchors and buried both within D channel at the Aquadopp location and on the flanking flats (Fig. 1). In addition, a HOBO U20 water level and temperature logger was positioned on the sand anchors at the flat's surface (0 cm) to obtain temperature and pressure measurements. The temperature was sampled every 5 min, more than twice the response time of the instruments. A string of temperature loggers was also attached to a piling at the mouth of D channel to measure conditions in the Bear River Channel. Pressure loggers at the top and bottom of the logger string were used to correct the pressure measurements from the Aquadopp and HOBO pressure loggers for atmospheric pressure to obtain accurate measurements of flow depth.

2.3. Remote sensing measurements: infrared images and LiDAR scans

An infrared (IR) imaging system was deployed on a 10 m tower attached to the D channel piling. IR data were collected at 7.5 Hz with a 320×240 pixel 16 bit $8-12$ μm thermal camera (FLIR A40) with a 39° horizontal field of view lens oriented along the channel axis. A 66° incidence angle provided an imaged area of approximately 100 m by 40 m and a horizontal resolution of O(1 cm) in the near-field degrading to O(2 m) in the far-field. The gradient in resolution is a result of perspective (Holland et al., 1997).

To calculate the surface velocities when the local water depth was below the Aquadopp 0.1 m blanking distance, a Fourier transform based method was used to convert the infrared signal into a time-series of surface velocities. This Optical Current Meter method has been successfully used to compute nearshore surface currents (Chickadel, 2003) and breaking wave speeds (Thomson and Jessup, 2009). This study extends the method to computing surface velocities in the shallow channel using the infrared video and is renamed the Infrared Current Meter (IRCM). Traditionally, IR techniques rely on the cool-skin effect to provide flow signatures. Because this study was performed during daytime with significant solar heating, the cool-skin effect was not observed. Instead, surface bubbles advecting with the flow formed the major signal during the deployment. The thin film of the bubble cools faster than the surface water creating a strong signal against the warm channel outflow. The IRCM technique follows the Optical Current Meter (OCM) of Chickadel (2003) and therefore only a brief overview will be given below.

The infrared data were georectified to a local coordinate system (Holland et al., 1997) to obtain a two-dimensional time series of pixel intensity with a resolution of 3.8 cm. After georectification, a 4 m slice (pixel array) of the imagery along the channel axis and just upstream of the Aquadopp was taken and converted into time stacks $I(t,x)$ (Fig. 2). Time stacks show the evolution of the video along a single line of pixels in time. In

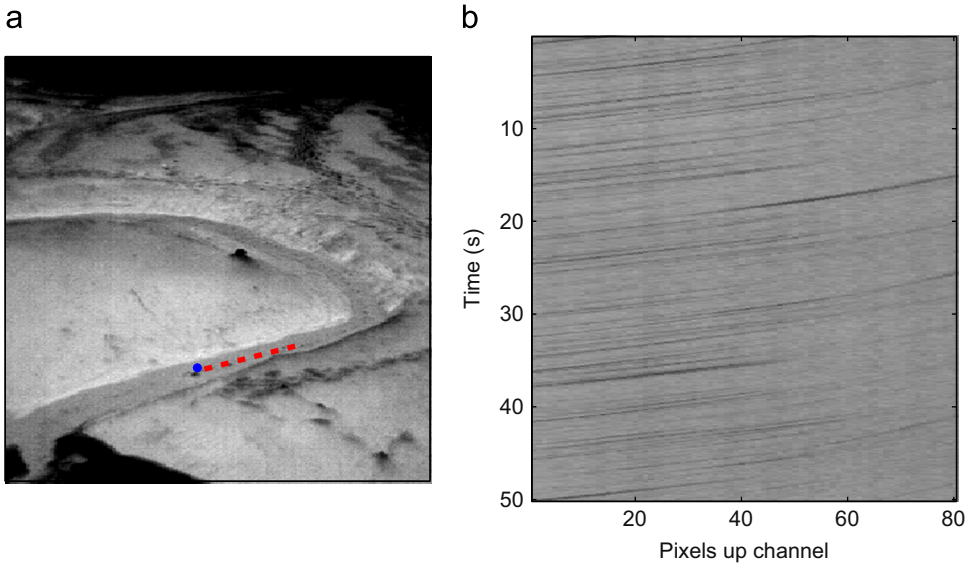

Fig. 2. (a) Example (unrectified) IR imagery of D channel from the tower at 10:30. Warmer regions are brighter. D channel curves from the left edge of the image to the right and drains into the cold (black) Bear River Channel at the bottom of the image. Dark spots within the channel are bubbles on the water surface while the dark spots on flats are footprints from the instrument deployment the previous day. The dark object in the center is a buoy on the flat surface used for rectification and the blue dot is the location of the Aquadopp. The red dashed line represents the pixel array used to generate the (b) timestack (time-series of pixel intensities) from the same time. The black streaks moving through the time stack are bubbles on the water surface.

practice, multiple lines are used to determine the surface currents at different positions across the channel. The pixel intensities were transformed into the frequency–wavenumber domain $\hat{I}(f,k)$ using a two-dimensional Fourier transform

$$\hat{I}(f,k) = \int\int B(t,x) I(t,x) e^{-i2\pi ft} e^{-i2\pi kx}\, dt\, dx \tag{1}$$

where f is the frequency (Hz), k is the wavenumber (m^{-1}), and $B(t,x)$ is a two-dimensional Bartlet filter (Press et al., 2007) to reduce spectral leakage. The spectral power, $S(f,k) = \hat{I}(f,k)\hat{I}^{*}(f,k)$, where the star (*) indicates the complex conjugate, was then computed and the spectrum was converted to velocity–wavenumber space using the mapping $v = fk^{-1}$. The transformation is

$$var\{S(f,k)\} = \int\int S(f,k)\, df\, dk = \int\int S(v,k)|k|\, dv\, dk \tag{2}$$

where $|k|$ is the Jacobian determinant and $S(v,k)$ is the velocity–wavenumber spectrum. Following this transformation preserves the variance of the signal. The frequency and wavenumber are constrained during this integration so that the velocities lie between $\pm 2\ ms^{-1}$.

Following the transformation to velocity–wavenumber spectrum $S(v,k)$, the velocity spectrum $S(v)$ is then obtained by

$$S(v) = \int_{k_{min}}^{k_{nyq}} S(v,k)\, dk \tag{3}$$

where $k_{nyq} = 1/2\ dy = 13\ m^{-1}$ is the Nyquist wavenumber and $k_{min} = 0.33\ m^{-1}$ was chosen to minimize bias from low wavenumber noise. The $S(v)$ spectrum was then fit to a model assuming a Gaussian velocity distribution combined with white noise to obtain an estimate of velocity for that spectrum and a 95% confidence interval for the velocity was determined from a nonlinear least squares fit (See Chickadel, 2003, for details). The video data were binned into 256 sample timestacks with 50% overlap and the above procedure run on each segment of video providing a timeseries of velocities with a period of 17.1 s from the initial 7.5 Hz video.

Additionally, a Riegl LMS-2210ii (905 nm) LiDAR was used to measure the elevation of the tidal flats. A scan was performed at low tide and gridded to a resolution of 10 cm. These data provided accurate measurements of the channel cross-sectional area to perform volume flux calculations (see Section 3). A larger-scale LiDAR dataset, obtained from USGS was used to estimate the size

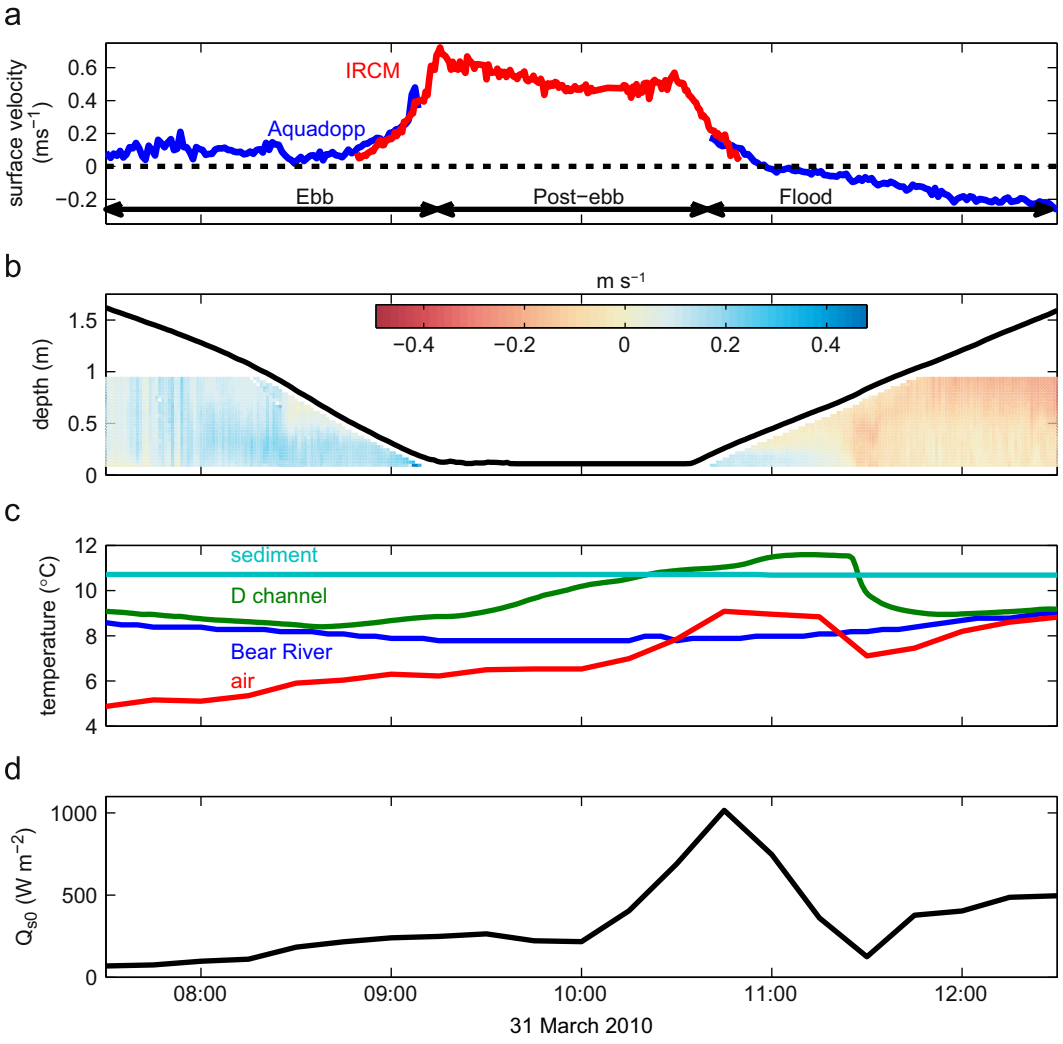

Fig. 3. Observed time series of (a) Aquadopp near-surface (blue) and IRCM surface (red) velocities, (b) water depth and along-channel velocity measured by the Aquadopp ADCP (c) temperature of the air (red), drainage water in D channel (green), sediment at depth (cyan) and in Bear River channel (blue), (d) incoming solar shortwave radiation Q_{s0}.

of the drainage basin captured by the 'D' channel during low tide exposure.

The channel bathymetry was constructed from the LiDAR scan taken at maximum low tide. As the 905 nm LiDAR cannot penetrate the water surface, some additional interpolation was required to reconstruct the full channel bathymetry. The portion of the channel occupied with water was identified and the center of the channel was assigned the measured water depth at the sand anchor that was co-located with the Aquadopp. The bathymetry of the inundated portion of the channel was then interpolated as a cubic spline fit to the exposed channel area.

3. Results

3.1. Channel currents and temperature

Along channel velocities from the co-located Aquadopp and IRCM measurements are shown in panels (a) and (b) of Fig. 3, along with tidal elevation. During the ebb, maximum observed velocities occur as the water level approaches the flat elevation of about 1 m relative to the channel bed at 08:00. This is consistent with the maximum rate of change in the instantaneous tidal prism (i.e., the volume of tide water) going from the flat to the channel and corresponds to the ebb pulse (Nowacki and Ogston, 2013). Across-channel velocities (not shown) in the lower meter are typically small, but may increase in the region above the 1 m sampling distance when the tidal elevation is above the flats and the tide propagates across the flats, as seen in Nowacki and Ogston (2013) and Mariotti and Fagherazzi (2011). At 09:15, the ebb passes the Aquadopp site and the measured water depth in the channel becomes constant at 0.1 m (the surrounding flats are exposed). The water in the channel continues to flow seaward, however the 0.1 m flow depth is within the acoustic blanking distance of the instrument. Although the pressure and temperature measurements are still valid, no useful Doppler velocity data are collected during this shallow flow. The IRCM shows that channel drainage continues and is characterized by a slow decrease in velocity (until the next flood tide when water from the Bear River Channel enters D channel).

When both the IRCM and Aquadopp measurements are valid, the measurements from the top bins of the Aquadopp compare well with the results of the IRCM technique (Fig. 4a). The overall correlation between the currents speeds is $r^2 = 0.82$. (Fig. 4). The 95% confidence intervals around the IRCM calculations span from ± 0.5 cm s^{-1} to ± 2.5 cm s^{-1} with a median of ± 1.7 cm s^{-1}. This is significantly smaller than the errors expected from the raw (1 Hz) Aquadopp which are O(10 cm s^{-1}). Fig. 4b also shows that surface velocities are well correlated with depth-averaged flow (panel b), suggesting that IRCM values, which are surface values by definition, can be used to estimate total discharge.

Also shown in Fig. 3 are water temperatures (panel c), which vary notably in the D channel during low tide relative to the values downstream in the Bear River. The temperature signal is useful to constrain the source of the drainage, which is either remnant surface water, exfiltrating porewater, or rainfall. Remnant water is expected to have a strong thermal response to external heat fluxes, because of a small thermal mass and direct exposure to solar heating, convection by wind, etc. Fig. 3 shows strong solar forcing (panel d) during the later stages of the post-ebb period. Thus, there are valid mechanisms for remnant water on the flats to undergo both the cooling and the heating necessary to produce the observed channel outflow temperatures. Porewater, by contrast, is expected to have a very weak thermal response, because saturated muddy sediment within the flats are well-insulated from external heat fluxes and have a large thermal mass (Thomson, 2010).

3.2. Channel current profiles

For the purpose of estimating the total discharge and associated open-channel flow dynamics, the important parameter is the depth and cross-sectionally averaged channel velocity $\overline{v}(t)$. Here, we use observations of the depth and cross-channel profiles, when available, to scale factors such that the mid-channel surface velocities $v_{surf}(t)$ can be applied at all times to obtain

$$\overline{v}(t) = \frac{1}{A}\int_A v(x,y,t)\, dA = C_x C_z v_{surf}(t) \tag{4}$$

where the integral is taken over the channel area A and C_x and C_z are the horizontal and vertical scale factors, respectively. As only a small subset of the data has observations with both cross-channel and depth profiles simultaneously, the scale factors are necessary to obtain volume flux measurements.

The Aquadopp measures vertical profiles of the velocity, as shown in Fig. 5 for select times. The profiles show unexpected sub-surface velocity maxima. Similar profiles have been observed in the late stages of channel drainage on other flats (Wells et al., 1990). Bottle samples taken from the channel outflow during these times show high suspended sediment concentrations, from 1.2 to 8.9 gL^{-1} at 08:42 and 10:15. Increased ADCP backscatter during these periods also suggests the presence of high

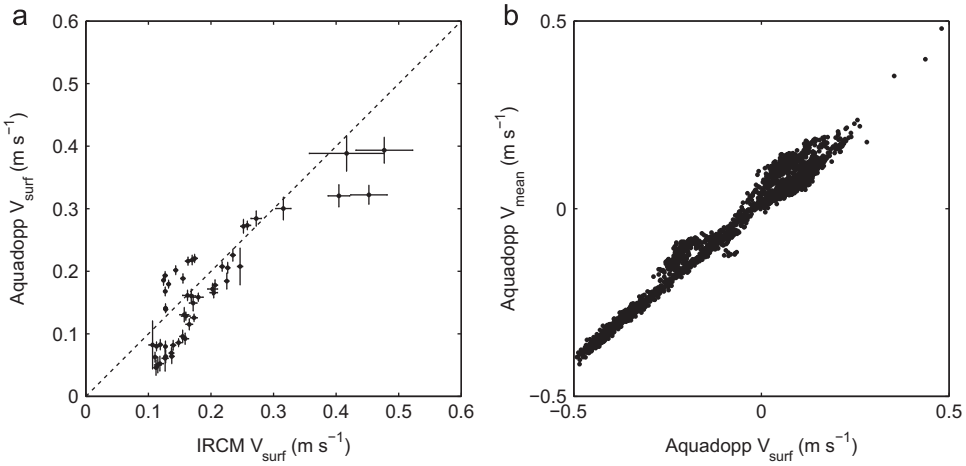

Fig. 4. (a) Comparison of Aquadopp and IRCM measured surface velocities. Error bars are 95% confidence intervals around the calculated IRCM velocities and the dashed line indicates one-to-one correspondence. (b) Comparison of Aquadopp surface velocities to depth-averaged velocities.

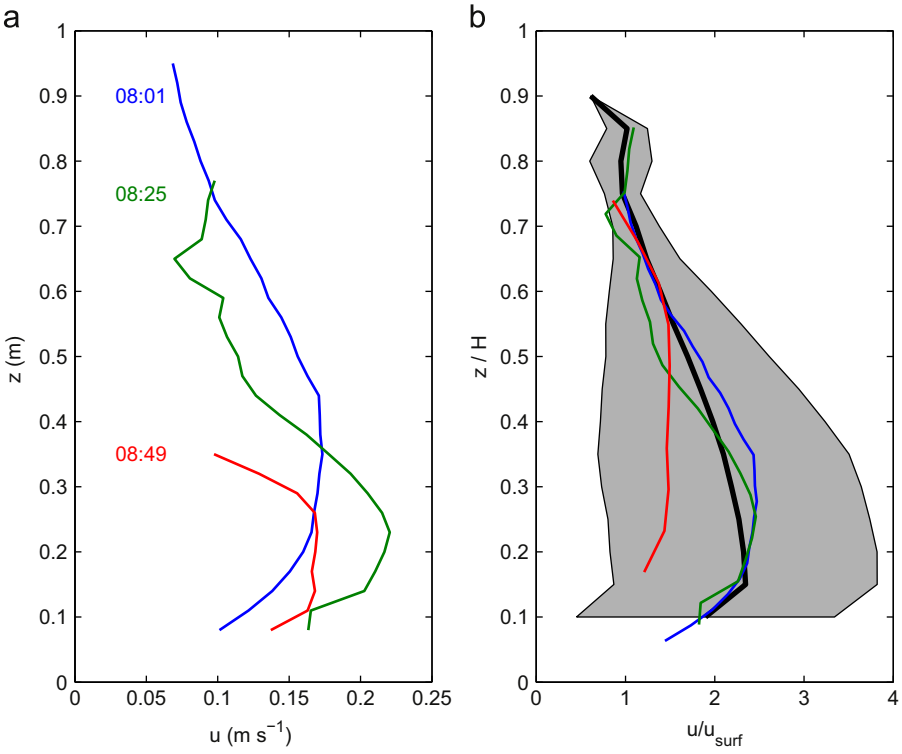

Fig. 5. (a) Depth profiles of surface outflow velocity from the Aquadopp at various times, and (b) corresponding normalized profiles. The thick black line is the mean for all profiles and the gray shading is the standard deviation.

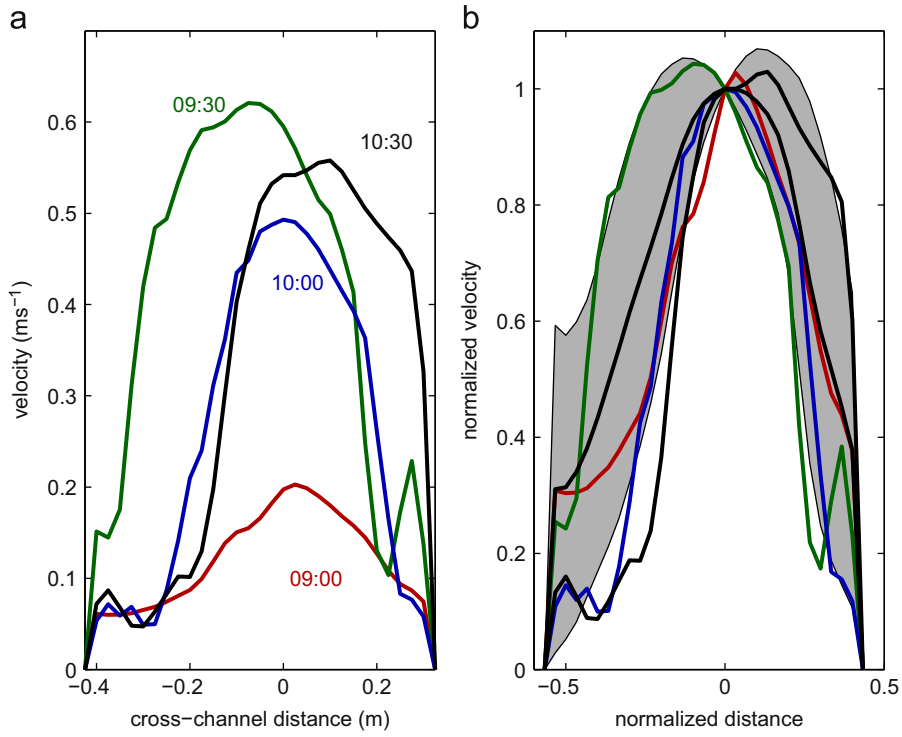

Fig. 6. (a) Cross-channel profiles of surface outflow velocity from the IRCM at different times, and (b) corresponding normalized profiles. The thick black line is the mean for all profiles and the gray shading is the standard deviation.

suspended sediment concentrations indicating the possibility of suspended sediment supported gravity flows. Although our sparse observations of suspended sediment concentration are insufficient to investigate the details of gravity flows, the quadratic fit describes the observations well and the high concentrations motivate the quantification of post-ebb drainage. Alternatively, surface stresses from wind and cross-channel circulation may be responsible for these sub-surface maxima.

The normalized velocity profiles are used to find the scalar constant C_z, which relates the observed surface velocity to the depth-averaged velocity, such that $1/h \int v(z)\,dz = C_z v_{surf}$. The factor C_z is thus the slope of the comparison in Fig. 4b. This depth correction factor is assumed to apply across the entire channel, however the surface velocities v_{surf} are allowed to vary across the channel.

The cross-channel variations in surface velocity v_{surf} are quantified using multiple IRCM lines are shown in Fig. 6 for selected times. The cross-channel profiles show an expected maxima mid-channel and a quasi-symmetric reduction near the channel side-walls, consistent with a no-slip condition along the walls. The normalized profiles are used to define a scalar constant C_x, which relates the observed surface velocity to the cross-channel-averaged velocity, such that $\int v(x)\,dx / \int dx = C_x v_{surf}$. The cross-channel correction factor is assumed to apply at all depths, however, the velocity may vary with depth (as determined in the preceding definition of C_z).

3.3. Total channel discharge

The discharge (i.e., volume flux) outflowing from D channel is estimated using the measured surface velocities and applying the scaled profile coefficients, such that

$$\mathcal{V}(t) = \int\int v(y,z,t)\,dy\,dz = \overline{v}(t)A(t) = C_y C_z v_{surf}(t)A(t) \quad (5)$$

where $v_{surf}(t)$ is the mid-channel surface measurement (from either the IRCM or the Aquadopp) at a given time, A is the channel cross-sectional area (determined from the Aquadopp pressure gauge and the extrapolated LiDAR scan) at a given time, and C_x, C_z are the scale factors adjusting the observed surface velocity to a channel- and depth-averaged value.

The channel discharge from Eq. (5) is shown in Fig. 7 on a log axis as a function of linear time. Discharge rapidly decreases during the end of the ebb and the rate of decrease slows during the post-ebb period. Generally, there is an exponential decay with time, consistent with the hydrographic recession of a drainage basin (Jones and McGilchrist, 1978; Brutsaert, 2005)

$$\mathcal{V}(t) = \mathcal{V}_0 e^{-\alpha t}. \quad (6)$$

Here the exponent α is determined to be approximately $3.7\ \mathrm{h}^{-1} \pm 0.54$ during the ebb and $1.5\ \mathrm{h}^{-1} \pm 0.08$ for the post-ebb flow. This change in exponent indicates a change in the underlying dynamics from the ebb-tidal-elevation driven flow to a uniform open channel flow regime during the post-ebb period. While a visual inspection of the plot seems to indicate a change in slope somewhere between 08:45 and 09:15, the dynamic analysis in Section 4.1 suggests 09:15 as the change in dynamic regime. For the purpose of this study, however, the exact time period does not significantly alter the results.

Integrating in time under the post-ebb discharge portion of the volume flux estimates gives a total outflow volume of approximately 400 m^3. Using the LiDAR data to delineate the upstream drainage basin, the upstream area is $A_{total} = 3 \times 10^5\ \mathrm{m}^2$ (see Fig. 1b). Combining these estimates indicates that the observed drainage in the D channel would require a skim of approximately $d \sim 1.3$ mm deep remnant water on the surface of the flats. Of course, it is unlikely that the remnant water is uniformly distributed across the observed flats, because ridges and runnels are common to muddy tidal flats (O'Brien et al., 2000; Gouleau et al., 2000; Whitehouse et al., 2000). A more realistic guess at the distribution of remnant water thickness is $d \sim$ 13–26 mm over 5–10% of the exposed flats, and this estimate is used in subsequent thermodynamic modeling of the remnant water (to predict channel discharge temperatures, see Section 4.2).

Porewater and rainfall are potential alternate sources of the post-ebb discharge. Estimating the total major channel length from the LiDAR as 2 km and a mean channel depth of 0.5 m, the hydraulic conductivity along the channel flanks would need to be 10^{-3} cms^{-1} (assuming unit hydraulic gradient, i.e. 1 m change in head over 1 m horizontal distance) to generate the observed fluxes of 0.2 $\mathrm{m}^3\ \mathrm{s}^{-1}$ via porewater discharge. This is well above the 10^{-6} to 10^{-9} cms^{-1} estimates of hydraulic conductivity within Willapa mud flats (B. Boudreau, personal communication), and thus is unlikely to contribute noticeably to the source of post-ebb drainage. Another potential source is rainwater. During this low tide two trace rainfall events occurred of less than 0.25 mm each for a maximum possible 0.5 mm. While its unlikely that the total rainfall was this high, this would still represent only half of the observed discharge.

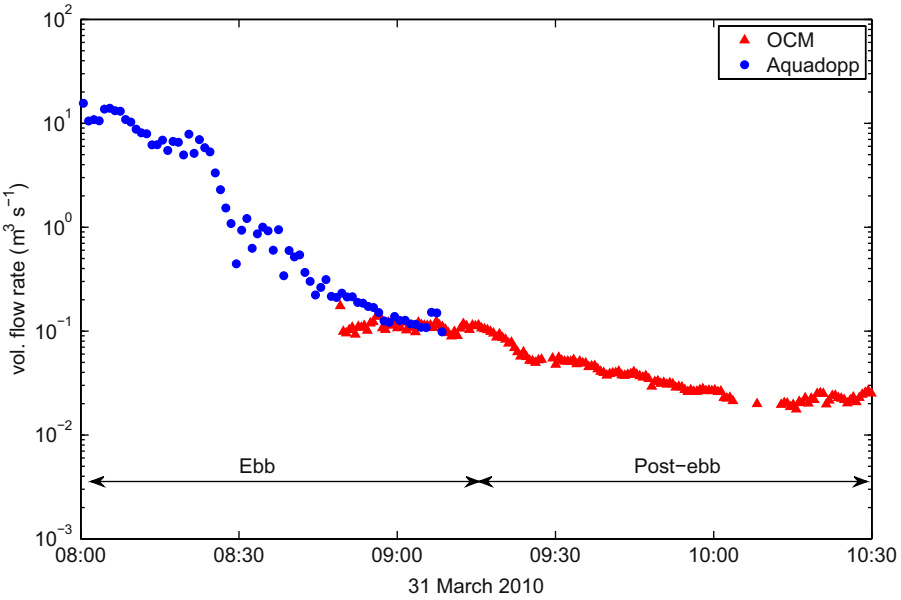

Fig. 7. Time series of discharge (total volume transport) as calculated from the Aquadopp (circles) and IRCM (triangles) techniques. Ebb and post-ebb discharge periods are indicated by the labeled arrows.

4. Discussion

4.1. Dynamic separation of tidal versus post-ebb discharge flows

A simple description for steady open-channel flow is the Gauckler–Manning Equation (Gioia and Bombardelli, 2002)

$$\overline{v} = \frac{k}{n} R_h^{2/3} S_f^{1/2} \tag{7}$$

where $\overline{v}$ is the mean velocity (depth- and cross-sectionally averaged), n is the Gauckler–Manning coefficient indicating the roughness of the channel, R_h is the hydraulic radius (the ratio A/p of the cross-sectional area A to the wetted channel perimeter p), k is a unit conversion factor equal to unity for SI units, and S_f is the friction slope, a function of the changing channel depth and the bed slope. This equation represents a balance between gravity (via slope) and friction (via roughness), assuming turbulent stress varies linearly as a function of distance to the channel boundary. Here, we use a Gauckler–Manning coefficient of $n=0.02$ (a typical value for natural mud), a LiDAR-based estimate of R_h, and $\overline{v} = \mathcal{V}(t)/A(t)$ where $\mathcal{V}(t)$ is calculated as in Section 3.3. The friction slope is then the only unknown variable.

The velocities $\overline{v}$ as a function of friction and hydraulic radius $nR_h^{-2/3}$ are shown in Fig. 8a, and the inferred friction slopes as a function of time in Fig. 8b. During the ebb period (prior to 09:15), the flow is directly proportional to $nR_h^{-2/3}$. From 09:00 to 09:15, S_f increases until the post-ebb discharge period. This increase in slope is consistent with the receding tide controlling the downstream water elevation creating a backwater effect at the measurement location.

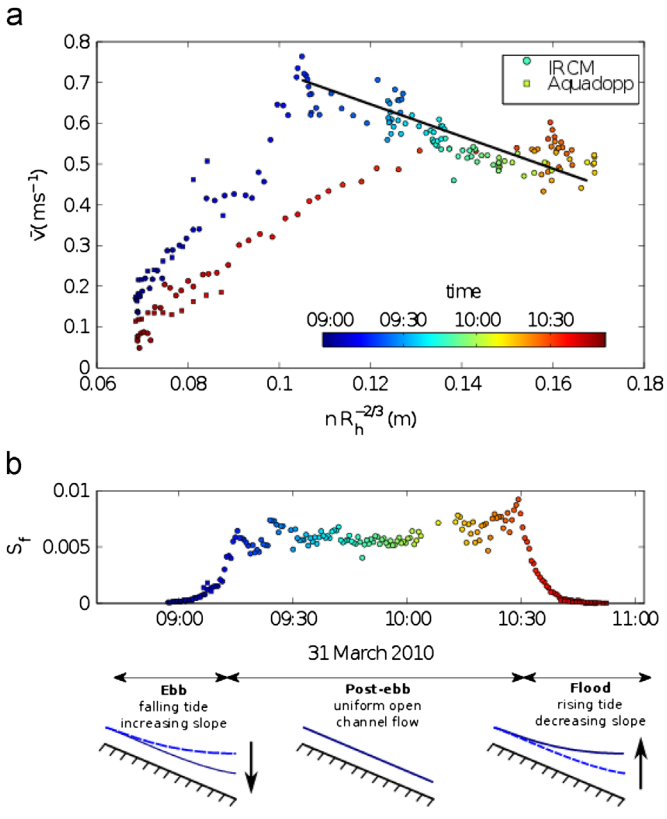

Fig. 8. (a) Depth-mean velocity vs $nR_h^{-2/3}$ from the Aquadopp (circle) and IRCM (square) datasets. Color corresponds to observation time. The line is a best-fit line for Eq. (7) for the post-ebb discharge period (after 09:15). (b) Calculated dynamic slope S_f during the same time period and schematic diagrams of the channel and water depth showing the influence of tidal elevation on channel slope. The dashed lines indicate the prior tidal elevation with the arrows showing rising or falling tide. The falling tide increases the friction slope S_f while the rising tide decreases S_f. During the post-ebb period, water elevation is steady and uniform throughout the channel with $S_f = S_0$.

As the downstream tidal elevation falls, the friction slope approaches a near constant value of $S_0=0.005$ during the post-ebb discharge period. If the flow is uniform in depth along the channel, then bed slope S_0 is equivalent to the friction slope, i.e. $S_0 = S_f$ and under these conditions the velocity is inversely proportional to $nR_h^{-2/3}$ with the slope of the regression equivalent to $S_0^{1/2}$. During the post-ebb period (after 09:15), the observations are consistent with uniform open channel flow and with an inferred bed slope of $S_0 = 0.005$, similar to nearby calculations of the actual channel slope by Mariotti and Fagherazzi (2011).

Following the post-ebb discharge period, the flood period shows a similar pattern to the ebb with $\overline{v}$ decreasing with $nR_h^{-2/3}$. The friction slope again decreases as the flooding tide increases downstream tidal elevations. It should be noted that while the velocities during the ebb and flood periods are influenced by the downstream tidal elevations they should still follow open-channel flow dynamics. In these situations, however, the flow depth is no longer uniform along the channel, nor is the flow steady. Instead, gradually varied flow dynamics would need to be considered and the friction slope would no longer be equivalent to the surface slope. Without precise measurements of the downstream elevations calculating the exact backwater conditions is difficult and beyond the scope of this experiment.

A simple schematic shown in Fig. 8 shows how the tidal flow influences the water elevation in the channel through the backwater effect of the downstream water elevation. As the tide recedes, the downstream elevation falls and S_f increases due to the increase in the water surface slope. This occurs until uniform open channel flow is established where the flow depth is the same everywhere and the water slope matches the bed slope. When the tide rises again the downstream tidal elevation reduces S_f and decelerates the flow. Dynamically, the ebb and post-ebb flow regimes differ in the importance of the bed and surface slopes in controlling the pressure gradient forcing. During normal tidal flow, the varying tidal elevation creates a water surface slope and hence a pressure gradient driving the flow. During the post-ebb discharge, however, when the flow depth is uniform along the channel, the bed slope is the main dynamic control on the pressure gradient.

4.2. Remnant water heat flux model

To further assess the hypothesis of remnant water on the flat surface as the source of post-ebb discharge in the channel, a heat-flux model is applied to predict the temperature of remnant water and then the predictions are compared with observed outflow temperatures. The model is necessary because remnant water temperatures on the flats were not measured directly, owing to the difficulties in measuring thin (O(1) mm) layers without disturbing the hydrodynamic system. Remnant water temperatures were not measured remotely, because the infrared field of view was too small to capture even a small fraction of the remnant water up on the flat.

Applying the model of Kim et al. (2010) and using the meteorological measurements, we estimate the near surface heat flux Q_{net} as

$$Q_{net} = Q_s + Q_l + Q_e + Q_h + Q_{sw} \tag{8}$$

where Q_s is net shortwave radiation, Q_l is net longwave radiation, Q_e is latent heat flux due to evaporation and freezing, Q_h is sensible heat flux, and Q_{sw} represents heat exchange between the sediment and water column during inundation of the flats. The main source of heat is the net shortwave radiation $Q_s = (1-\alpha)Q_{s0}$ where Q_{s0} is the

incoming solar shortwave radiation and α is the albedo of the water surface. A constant albedo of $\alpha = 0.08$ was used for this model, consistent with prior heat modeling experiments (Guarini et al., 1997). Q_l, Q_e, and Q_h generally represent losses of heat and are empirical functions of local meteorological conditions, modeled following Kim et al. (2010).

The sediment temperatures with depth in the sediment bed were also modeled following Kim et al. (2010) using the one-dimensional heat conduction equation

$$\frac{\partial T_s}{\partial t} = \kappa \frac{\partial^2 T_s}{\partial z^2} \tag{9}$$

where $T_s(z)$ is the sediment temperature with depth in the sediment z and κ is the sediment heat diffusivity. Previous work by Thomson (2010) found sediment thermal diffusivities ranging from 0.2 to0.7×10^{-6} m^2 s^{-1}. For this model a constant diffusivity of $\kappa = 0.5 \times 10^{-6}$ m^2 s^{-1} was used. Sediment temperatures were modeled to 1 m depth and initialized using the sand anchor observations. No heat fluxes were assumed to occur through the bottom boundary, while heat fluxes through the sediment-water interface were modeled as

$$Q_{sw} = H_{sw}(T_s - T_w) \tag{10}$$

where T_s and T_w are the sediment and water temperatures respectively. H_{sw} is the sediment–water heat transfer coefficient, with a constant value of 20 WK^{-1} m^{-2} used for this study. Values from 10 to 70 WK^{-1} m^{-2} were also tested and had little effect. This is likely due to the fact that the modeled locations were inundated during the entire time period allowing the sediment–water interface to come into a thermal equilibrium.

The temperature T of the remnant water that would be available to runoff into D channel is estimated using the net heat flux Q_{net} as a function of time t

$$\frac{\partial T(x,t)}{\partial t} = \frac{Q_{net}(t)}{C_v d} \tag{11}$$

where C_v is the volumetric heat capacity of seawater, and d is the depth of the water. The final temperature predictions $T(x,t)$ were obtained by time-integrating Eq. (11) for all t after the ebb has passed at given x value (i.e., once the flats are exposed and remnant water is left on the surface of the flats at a given location).

The model was applied at 11 vertical locations on the flat from 1.5 to 2.5 m above the channel mouth elevation and the tidal elevation from the sand anchor pressure gauge at the Aquadopp site was used to determine water depths at the modeled locations. We assumed a remnant water thickness $d = 0.01$ m, based on visual observations during fieldwork, in order to simulate the remnant water on the flat surface when the tidal elevation was below the flat elevation. The model was started at 00:00 31 March 2010, during a period of inundation prior to the IRCM observations and initialized with observed water and sediment temperatures of 9.8 °C, which were in equilibrium.

The model results for temperature and the heat fluxes are shown in Fig. 9. The heat flux terms for the mid-flat site (at 2 m above D channel mouth elevation) are representative of the whole system and are presented in Fig. 9b. At the mid-flat site, Q_{net} begins negative (predicting cooling of remnant water) and transitions to positive (predicting warming of remnant water) during

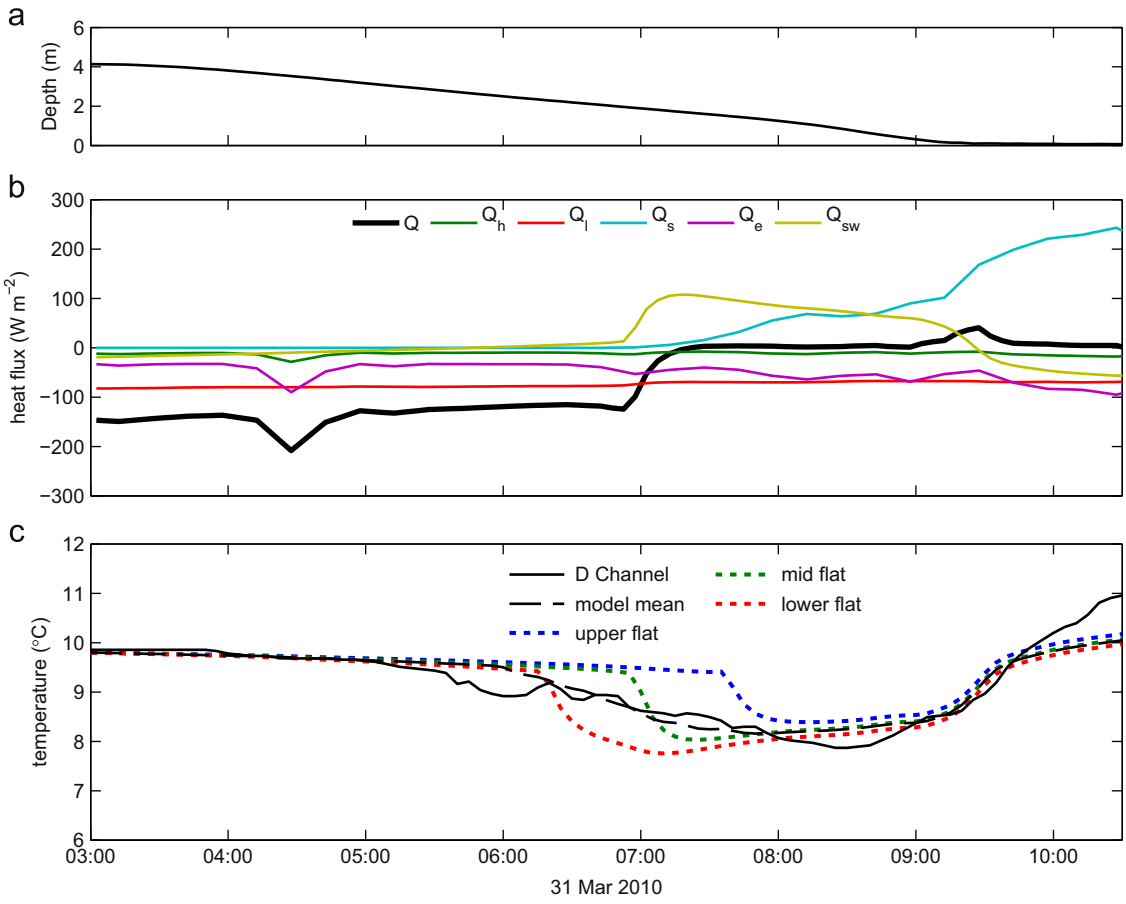

Fig. 9. (a) Time series of water level, (b) terms in the heat flux model (colored lines), and (c) resulting predictions of remnant water temperatures at different locations on the flats. The mean from the model regions (dashed line) compares well with the measured temperature of water in D channel (solid line). The upper, mid, and lower flats are located at 2.5 m, 2 m, and 1.5 m above the D channel elevation.

the drainage period. The key term for cooling remnant surface water is the long wave (blackbody) radiation Q_l, although some of the lost heat is replaced by warming from the positive exchange with the underlying mud (which has a large thermal mass and maintains 9.8 °C throughout most of the model time series). The key term for heating is solar radiation Q_s, which becomes dominant after 09:00.

The resulting estimates of remnant water temperature at representative locations on the flats are shown in Fig. 9. The upper, mid, and lower flat elevations are at 2.5 m, 2 m, and 1.5 m above the channel mouth elevation. Water on the upper flats initially cools under negative heat flux, then warms later when solar radiation increases. The mid and lower flat locations begin to cool later than the upper flat location, because they are exposed later. All locations begin warming together, largely driven by solar radiation, at 08:00.

The temperature signal in the channel is expected to lag the temperature signal of remnant water on the flats by the travel time required to reach the channel mouth. This lag will vary with flat location and runoff speed. Likely, the water in the channel is mostly remnant water from the nearest (and most recently exposed) portion of the flats. For the O(0.5 m s^{-1}) flows observed in the channel, the lag time over a distance of 100 m is only 200 s, which cannot be distinguished from Fig. 9. Lacking direct observations of the runoff velocities on the flats and in the runnels, we use a simple instantaneous mean of the modeled remnant water from all locations and compare to the observed temperatures at the same time. During the post-ebb period that is our focus (09:15–10:15), the modeled remnant water temperatures are similar at all locations, so the choice of position and associated time lag is not significant to the overall inference that channel drainage temperature is consistent with predictions for the temperature of remnant surface water.

The overall trend of cooling and then warming closely matches the observed drainage temperatures in D channel, which are highly variable relative to the constant Bear River channel water temperatures or constant mud temperatures (see Fig. 3). If, instead, the channel drainage source was porewater, the drainage temperature would be closer to a constant 10.8 °C, which is the temperature observed from the buried (0.5 m) HOBO loggers within the mudflats. The heat flux model demonstrates that the temperature measurements are consistent with a thin film of water running off of the flats and undergoing the expected thermal changes associated with this runoff and eventual conveyance through D channel.

5. Conclusions

Using a combination of in situ and remote measurements, we have quantified drainage in the channel of a natural tidal flat. The IRCM technique provides accurate measurements of surface velocity that compare well with in situ ADCP measurements. Parametric current profiles are fit to obtain estimates of volume flux along the channel, and the corresponding mean flows are assessed with the Gaukler–Manning equation. Temperature observations in the channel are consistent with predictions for the runoff of $\mathcal{O}(10^{-2}$ m) thick surface remnant water that cools after initial exposure and then warms via solar radiation.

The dynamics of the observed drainage were separated into two regimes: ebb tide and post-ebb discharge. The Gaukler–Manning equation for open channel flow accurately describes both of these regimes through variations in surface and bed slopes. During the ebb tidal flow, a decrease in tidal elevation causes an increasing water surface slope and thus increasing velocities. In the post-ebb discharge regime, flow is uniform (constant-depth) down a bed slope and velocity slowly decreases as water mass is lost from the flats. These results may be applied in future studies to estimate discharge in the absence of measurements.

Low tide discharge from mudflats is a mechanism for downstream transport of material (and heat) that is often ignored, in part because it is difficult to measure. Although small, the long-term implication of this downstream transport may be significant in setting the morphology of the flat. Clearly, more study is necessary to understand the importance of post-ebb drainage. Future improvements would be to understand the spatial variability of remnant water on the flats, and to map pathways of the runoff through runnels and into channels. Additionally, detailed measurements of sediment concentrations during these periods would provide estimates of off-flat sediment flux.

Acknowledgments

Thanks to E. Williams for assisting in LiDAR data collection and deployment. A. de Klerk built and tested the sand anchor temperature profiles. J. Talbert built the imaging tower. Thanks to the Applied Physics Lab field team: A. de Klerk, J. Talbert, and D. Clark. Steve Elgar and Britt Raubenheimer (WHOI) provided the LiDAR used in this study. The Washington State University AgWeatherNet program collected and disseminated the Meteorological data. USGS performed the airborne LiDAR surveys of Willapa Bay. Thanks also to several anonymous reviewers of earlier versions of the manuscript. Funding provided by ONR Grant N000141010215.

References

Allen, J.R.L., 1985. Intertidal drainage and mass-movement processes in the Severn Estuary: rills and creeks (pills). Journal of the Geological Society 142, 849–861.

Anderson, F., Howell, B., 1984. Dewatering of an unvegetated muddy tidal flat during exposure—desiccation or drainage? Estuaries 7, 225–232.

Andrews, R., 1965. Modern Sediments of Willapa Bay, Washington: A Coastal Plain Estuary. Technical Report Number 118, University of Washington, Seattle, WA.

Ashley, G.M., Zeff, M.L., 1988. Tidal channel classification for a low-mesotidal salt marsh. Marine Geology 82, 17–32.

Banas, N., Hickey, B., MacCready, P., Newton, J., 2004. Dynamics of Willapa Bay, Washington: a highly unsteady, partially mixed estuary. Journal of Physical Oceanography 34, 2413–2427.

Brutsaert, W., 2005. Hydrology: An Introduction. Cambridge University Press.

Chickadel, C.C., 2003. An optical technique for the measurement of longshore currents. Journal of Geophysical Research 108, 3364.

Fagherazzi, S., Mariotti, G., 2012. Mudflat runnels: Evidence and importance of very shallow flows in intertidal morphodynamics. Geophysical Research Letters 39.

Gioia, G., Bombardelli, F., 2002. Scaling and similarity in rough channel flows. Physical Review Letters 88, 6465.

Gouleau, D., Jouanneau, J., Weber, O., Sauriau, P., 2000. Short-and long-term sedimentation on Montportail–Brouage intertidal mudflat, Marennes–Oleron Bay (France). Continental Shelf Research 20, 1513–1530.

Guarini, J., Blanchard, G., Gros, P., Harrison, S., 1997. Modelling the mud surface temperature on intertidal flats to investigate the spatio-temporal dynamics of the benthic microalgal photosynthetic capacity. Marine Ecology Progress Series 153, 25–36.

Gutiérrez, J., Iribarne, O., 2004. Conditional responses of organisms to habitat structure: an example from intertidal mudflats. Oecologia 139, 572–582.

Holland, K., Holman, R., Lippmann, T., Stanley, J., Plant, N., 1997. Practical use of video imagery in nearshore oceanographic field studies. IEEE Journal of Oceanic Engineering 22, 81–92.

Jones, P., McGilchrist, C., 1978. Analysis of hydrological recession curves. Journal of Hydrology 36, 365–374.

Kim, T.W., Cho, Y.K., You, K.W., Jung, K.T., 2010. Effect of tidal flat on seawater temperature variation in the southwest coast of Korea. Journal of Geophysical Research 115.

Kleinhans, M.G., Schuurman, F., Bakx, W., Markies, H., 2009. Meandering channel dynamics in highly cohesive sediment on an intertidal mud flat in the Westerschelde estuary, the Netherlands. Geomorphology 105, 261–276.

Le Hir, P., Roberts, W., Cazaillet, O., Christie, M., Bassoullet, P., Bacher, C., 2000. Characterization of intertidal flat hydrodynamics. Continental Shelf Research 20, 1433–1459.

Mariotti, G., Fagherazzi, S., 2011. Asymmetric fluxes of water and sediments in a mesotidal mudflat channel. Continental Shelf Research 31, 23–36.
Nowacki, D.J., Ogston, A.S., 2013. Water and sediment transport of channel-flat systems in a mesotidal mudflat: Willapa Bay, Washington. Continental Shelf Research 60S, S111–S124.
O'Brien, D., Whitehouse, R., Cramp, A., 2000. The cyclic development of a macrotidal mudflat on varying timescales. Continental Shelf Research 20, 1593–1619.
Peterson, C., Scheidegger, K., Komar, P., Niem, W., 1984. Sediment composition and hydrography in six high-gradient estuaries of the northwestern United States. Journal of Sedimentary Research 54, 86–97.
Press, W.H., Teukolsky, S.A., Vetterling, W.T., 2007. Numerical Recipes. The Art of Scientific Computing, third ed. Cambridge University Press.
Ralston, D., Stacey, M., 2007. Tidal and meteorological forcing of sediment transport in tributary mudflat channels. Continental Shelf Research 27, 1510–1527.
Thomson, J.M., 2010. Observations of thermal diffusivity and a relation to the porosity of tidal flat sediments. Journal of Geophysical Research 115.
Thomson, J.M., Jessup, A., 2009. A Fourier-based method for the distribution of breaking crests from video observations. Journal of Atmospheric and Oceanic Technology 26, 1663–1671.
Uncles, R.J., Stephens, J., 2011. The effects of wind, runoff and tides on salinity in a strongly tidal sub-estuary. Estuaries and Coasts 34, 758–774.
Wells, J., Adams Jr, C., Park, Y., Frankenberg, E., 1990. Morphology sedimentology and tidal channel processes on a high-tide-range mudflat, west coast of South Korea. Marine Geology 95, 111–130.
Whitehouse, R., Bassoullet, P., Dyer, K., Mitchener, H., Roberts, W., 2000. The influence of bedforms on flow and sediment transport over intertidal mudflats. Continental Shelf Research 20, 1099–1124.
Wood, R.G., Black, K.S., Jago, C.F., 1998. Measurements and preliminary modelling of current velocity over an intertidal mudflat, Humber estuary, UK. Geological Society, London, Special Publications 139, 167–175.